

OPTIMIZATION OF INTERCONNECTED 3D-PRINTED STRUCTURES FOR UAVS

Chris D. Scott[1], Anthony M. Comer[1], Jay C. Hanan[1], and Alex Nunley[1]

[1]School of Mechanical and Aerospace Engineering, Oklahoma State University, Tulsa, OK, 74106

Abstract

This work evaluates a modular fused filament fabrication (FFF) workflow for replacing a carbon fiber VTOL boom on an X200 eVTOL hybrid UAV. Finite element analysis was used to generate stress fields for topology optimization (TO) and variable-thickness lattice (VTL) design. Because the boom exceeded typical print volumes, modular joint architecture was evaluated as a primary design variable. Joint testing showed that a pinned sleeve joint most closely approached homogeneous-beam behavior. The best topology-optimized boom design weighed 281 g and supported a 115.7 N load, corresponding to approximately FoS = 4.62. However, an aggressively reduced 193 g design failed by lateral rolling, revealing sensitivity to unmodeled off-axis loading. A final 218 g variable-thickness Kelvin lattice boom with a pinned sleeve joint was fabricated and validated using powered thrust testing. This design survived both the 5400 RPM X200 VTOL takeoff condition and a 6000 RPM maximum test condition. The results demonstrate that modular FFF boom replacement is feasible for the evaluated X200 load case when joint robustness, cross-sectional bending efficiency, and lattice load-path redundancy are designed together. Although the final printed boom remained 31% heavier than the 166 g carbon fiber baseline, it provides a viable feasibility demonstration for rapid, repairable UAV structural development.

Keywords: topology optimization; variable-thickness lattice; fused filament fabrication; UAV structures; modular design.

1. Introduction

Lightweight structural design is critical for UAV performance. Topology optimization has proven effective in reducing weight by concentrating material along load paths [1]. Additive manufacturing (AM) further enables these complex geometries with minimal tooling and has been used extensively in aerospace applications for UAV development as of late [2-17]. For example, Yap *et al*. demonstrated that topology-optimized micro-drone frames printed with AM achieved ≈90% mass reduction without sacrificing integrity [1]. Likewise, Müller and Gollnick noted that 3D printing “revolutionized” UAV prototyping by making design flexible and cost-effective, rapidly producing lightweight robust components [18]. However, Fused Filament Fabrication (FFF) is typically constrained by printer build volume. To create large Group 2 UAV parts on standard printers, our approach segments designs into interlocking modules. To date, hybrid structures with composite beams and printed material elsewhere are common in aerospace [18].

PLA polymer was selected for printing. The ability to rapidly fabricate spare components is also an advantage: García-Tíscar *et al*. emphasized that in-field replacement of damaged UAV parts by AM is highly desirable [20]. The proposed approach leverages these benefits by printing interchangeable PLA

segments for a larger airframe while upholding the stiffness-to-weight ratio benefits of topology optimization.

Many Group 1–2 unmanned aerial vehicles rely on carbon fiber composite spars, stringers, and stiffeners as their primary load-bearing structural elements [21]. These components are typically selected for their high specific stiffness and strength, enabling slender airframes with adequate margins under aerodynamic and inertial loading. However, such structural members are often geometrically simple, load-path dominated, and repeated across platforms, limiting design options, but making them well suited for computational design optimization. The workflow proposed in this study, combining stress-field-driven optimization with modular fused filament fabrication, may offer a viable alternative manufacturing pathway with and increase in design freedom for such components. In particular, spars and booms with well-defined load cases could theoretically be redesigned as stress field-optimized, additively manufactured structures that preserve required stiffness and strength while enabling rapid iteration, part consolidation, and reduced manufacturing complexity.

It is also worth noting that carbon fiber composite structures used in Group 1–2 UAV applications are frequently designed with substantial strength and stiffness margins to accommodate uncertainty in loading, manufacturing variability, and certification requirements. Conservative knockdown factors and factors of safety are commonly applied to composite design allowables for advanced aerospace applications [22]. While these margins are appropriate from a safety and reliability standpoint, they can easily exceed the demands of many operational missions. As a result, there exists the possibility that certain carbon fiber spars, stiffeners, and booms are stronger than necessary for their intended load envelopes. Under such conditions, alternative structural concepts, such as optimized, additively manufactured polymer structures, could theoretically satisfy performance requirements while offering advantages in cost, manufacturability, and design flexibility. This study does not seek to replace carbon fiber composites in all applications, but rather to explore whether a subset of Group 1–2 UAV structural components might be addressed using a different design and manufacturing paradigm.

This work integrates nTop-based stress analysis, field-driven topology optimization, variable-thickness lattice design, modular FFF fabrication, and experimental structural evaluation. The vast majority of similar work focuses on small-scale homogeneous UAV structures [1,23]. This work is novel in that it combines large-scale topology optimization and variable-thickness lattice design with mechanically joined segmented FFF-printed UAV structures. Reliability considerations are addressed through structural analysis, joint characterization, boom-level loading, and failure-mode evaluation of joined PLA structures under representative loading conditions. The study first establishes the numerical modeling and optimization workflow, then experimentally evaluates candidate joint architectures, and finally applies the selected joining strategy to boom-level structural demonstrations. The results are used to identify the design tradeoffs between topology optimization, variable-thickness lattice design, joint robustness, cross-sectional bending efficiency, and carbon fiber mass equivalency.

2. Methods

2.1 X200 Platform, Load Case, and Replacement Objective

The representative platform used in this study was the X200, a Group 2 electric vertical takeoff and landing (eVTOL) hybrid UAV. The aircraft has an approximate vehicle weight of 8.16 kg and uses carbon fiber boom members to transfer VTOL motor loads into the wing and spar assembly. The baseline carbon fiber boom assembly had a measured mass of 166 g, including the bolts required for installation. The VTOL boom was selected as the initial replacement target because it is a repeated, load-path-dominated structural member and is therefore well suited for computational redesign and modular fabrication.

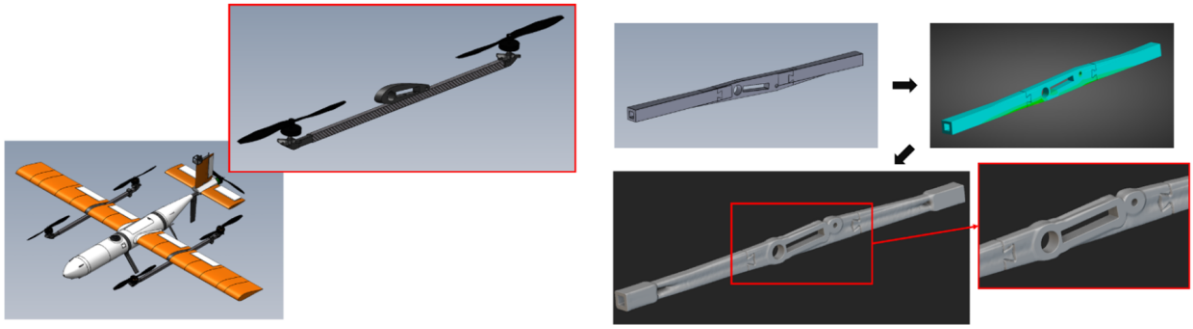


Figure 2.1 – X200 Group 2 eVTOL hybrid UAV with the baseline carbon fiber VTOL boom and printed replacement region identified.

A preliminary structural case study of the existing carbon fiber boom that the baseline boom was substantially overdesigned for the representative load case considered in this work. Therefore, the objective of the printed boom study was not to reproduce the full reserve capacity of the carbon fiber member. Instead, the objective was to determine whether a modular FFF polymer boom could provide a more practical structural margin, approximately in the FoS = 3–7 range, while improving manufacturability, repairability, and design flexibility.

The primary design load case was maximum vertical thrust during VTOL operation. This condition was selected because the boom transfers lift-motor thrust into the wing and spar assembly, producing a bending-dominated load state. To define a reference load, a thrust margin of 1.25 times the vehicle weight was used:

$$F_{total,req} = 1.25W \tag{1}$$

For the 8.16 kg X200,

$$F_{total,req} = 1.25(8.16\ kg)(9.81\frac{m}{s^2}) = 100.0\ N \tag{2}$$

With four VTOL propulsors, the corresponding required thrust per propulsor is

$$F_{prop,req} = \frac{F_{total,req}}{4} = 25.0\ N \tag{3}$$

The experimental boom factor of safety was therefore defined as

$$FoS = \frac{F_{applied}}{F_{prop,req}} \tag{4}$$

where $F_{applied}$ is the load applied at the motor/boom location. Static validation loads of 57.8 N and 115.7 N per evaluated boom side corresponded to approximate factors of safety of 2.31 and 4.62, respectively. The 57.8 N condition was used as an initial feasibility screen, while the 115.7 N condition represented a more demanding structural validation case within the desired design-margin range.

The carbon fiber wing spars were retained for the boom-level tests so that the boom replacement concepts could be isolated. Spar replacement is reserved for future work because it requires a separate cross-sectional flexural rigidity and buckling study for FFF-compatible spar geometries.

2.2 FEA, Material Model, and Optimization Workflow

Finite element analysis was used to generate the stress field that drove both the topology-optimized and variable-thickness lattice boom designs. All finite element simulations were conducted in nTop using a static structural framework. The boom root was constrained at the spar-hole interfaces to represent load transfer into the wing/spar assembly, and a load was applied in the +y-orientation at the distal motor mounting region to represent maximum VTOL thrust. For optimization, the applied load was 50.0

N at the motor mounting region, corresponding to the per-side thrust associated with a total lift capacity of 20.4 kg, or approximately FoS = 2 relative to the 10.2 kg reference lift requirement.



Figure 2.2 – FEA boundary conditions imposed on the boom design space (red: fixed spar-hole interfaces, and yellow: thrust load at the motor mounting regions).

The printed PLA material was modeled as a homogenized orthotropic linear elastic material to account for the direction-dependent stiffness introduced by FFF. The material axes were aligned with the global print directions used for the evaluated boom designs. This continuum representation was selected to capture the first-order anisotropic response of printed PLA without explicitly modeling individual beads, interlayer welds, voids, or raster discontinuities.

Table 2.1 – Homogenized orthotropic PLA properties.

Property	**PLA**
$E_1 = E_2$ (GPa)	3.2
E_3 (GPa)	1.8
ν_{12}	0.36
$\nu_{23} = \nu_{13}$	0.30
G_{12} (GPa)	1.18
$G_{23} = G_{13}$ (GPa)	0.69
ρ (kg/m^3)	1240

The finite element mesh used tetrahedral solid elements to accommodate the complex boom geometries generated during topology optimization and lattice design. A nominal element size of 3 mm was used with a mesh growth rate of 2. This mesh setting provided sufficient resolution at the motor mounting region, spar-hole interfaces, joint regions, and optimized structural members while maintaining reasonable computational cost for iterative design studies. A mesh convergence check was performed by refining the global element size and comparing changes in peak Von Mises stress and maximum displacement. The final 3 mm nominal element size was selected after these quantities stabilized to within an acceptable engineering tolerance, indicating that the stress field used to drive optimization was not dominated by mesh discretization.

The Von Mises stress field from the baseline design envelope was used as the scalar driving field for optimization. Although Von Mises stress is not a complete failure criterion for printed PLA, it provided a practical stress-intensity measure for identifying dominant load paths and regions requiring reinforcement. The baseline stress field was used in two design pathways: density-based topology optimization and variable-thickness lattice design.

Topology optimization was performed using a compliance-minimization objective to maximize stiffness under the prescribed maximum-thrust load case. The aggressive PLA boom designs used a volume fraction constraint of approximately 15%, with a maximum of 100 solver iterations. The convergence criteria were a minimum objective change of 0.0005 and a minimum localized density change of 0.01. After optimization, the output geometry was post-processed using Boolean operations to restore and thicken functional regions, including motor mounting pads, spar interfaces, and modular joint surfaces.

The variable-thickness lattice workflow used the same stress-field logic but retained a distributed internal architecture rather than removing material into sparse load paths. The final VTL boom used a Kelvin lattice with a 30 mm × 30 mm × 30 mm unit cell, a minimum lattice thickness of 0.8 mm, a maximum thickness of 5 mm, and a 1 mm exterior shell. Higher-stress regions were assigned thicker

lattice members, while lower-stress regions retained thinner members to reduce mass. This approach was intended to preserve load-path redundancy while still using FEA-derived material placement.

The topology-optimized designs were used for boom Designs 1–5. The variable-thickness lattice workflow was used for final Design 6 after the topology-optimized iterations showed sensitivity to joint design, cross-sectional stiffness, and off-axis loading.

2.3 Modular Segmentation and Joint Testing

The optimized boom geometries exceeded the available FFF build volume and were therefore segmented into printable modules. Modular segmentation enabled the fabrication of longer UAV structural members using accessible FFF equipment, but it also introduced joints that had to transfer bending, shear, and local bearing loads across printed interfaces. The joint architecture was therefore treated as a primary structural design variable rather than as a secondary assembly feature.

Candidate joints were designed to compare different load-transfer mechanisms, including geometric interlock, lap engagement, sleeve-supported bearing, and pin-assisted mechanical locking. Seven joint concepts were evaluated against a homogeneous no-joint beam: dovetail, double lap, rotated double lap, rotated double lap with two tabs, X joint, sleeve, and pinned sleeve. Each joint was tested in both X and Y orientations to evaluate directional performance.

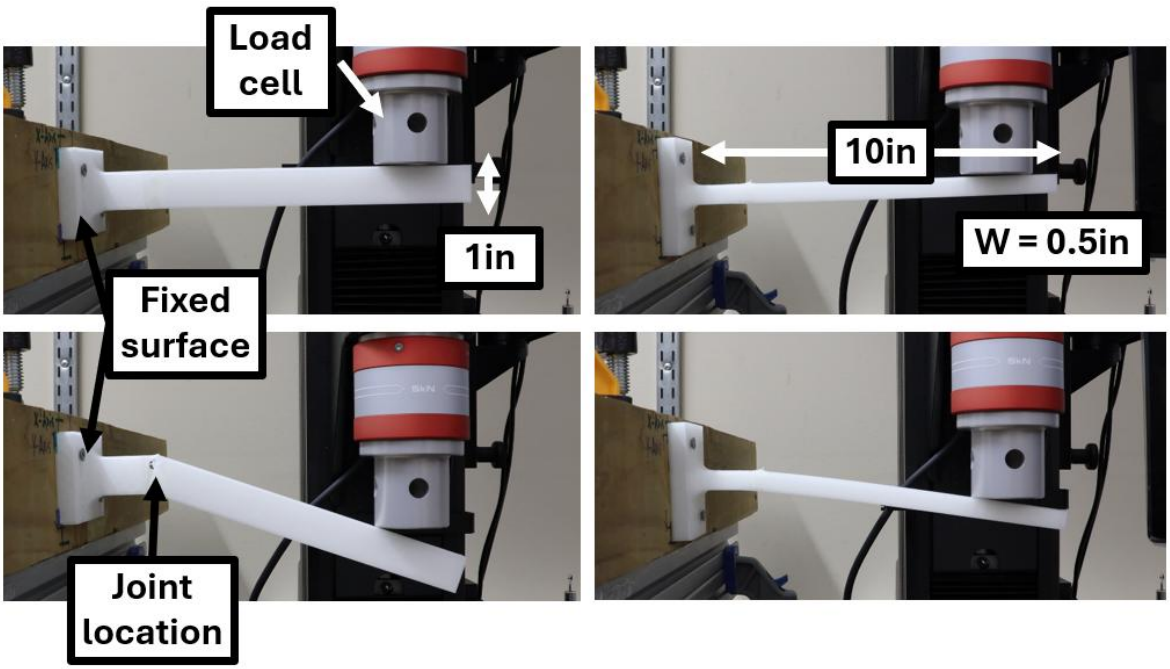


Figure 2.3 – Instron compression test setup for X (right) and Y-orientation (left) loading (top: preload, bottom: post load failure).

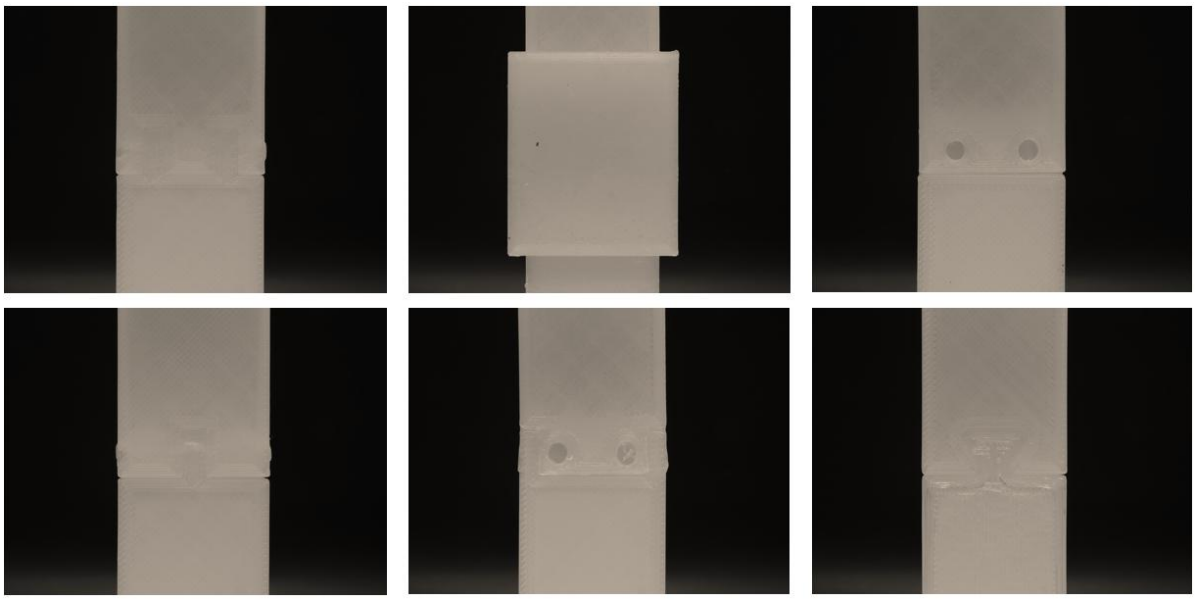


Figure 2.4 – Candidate joint geometries (Top left to right: Rotated double lap with 2 tab, sleeved, and double lap. Bottom left to right: Rotated double lap, X joint, and dovetail).

Initial joint specimens used an 8 mm lengthwise feature allowance. The best-performing or mechanically relevant designs were then retested at an increased 18.55 mm feature length to evaluate scale effects and determine whether increased engagement length improved load transfer. All joint coupons were printed in PLA using a 0.4 mm nozzle, 15% grid infill, and five perimeter walls. These print settings were held constant across the joint matrix so that geometry-driven performance differences could be isolated.

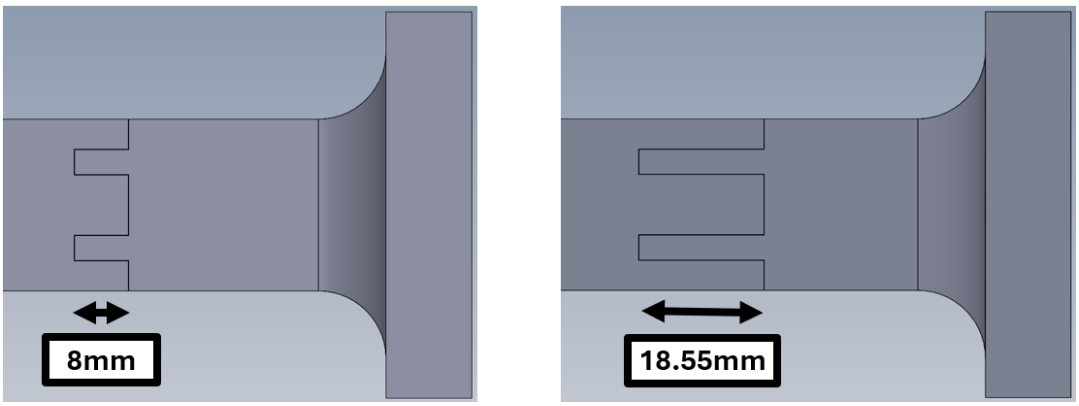


Figure 2.5 – Small- and large-scale lengthwise difference for joint testing (rotated double lap with two tabs pictured).

Joint performance was evaluated using maximum force, stiffness, displacement at maximum force, failure mode, and a structural efficiency index (SEI). The structural efficiency index ($\frac{kN^2}{mm}$) was defined as:

$$SEI = F_{max}k \tag{5}$$

where F_{max} is the maximum force supported by the specimen and k is the measured stiffness from the approximately linear region of the force-displacement response. This metric rewards joints that provide both high load capacity and high stiffness. The homogeneous beam served as the reference condition for evaluating how closely each modular joint approached continuous-member behavior.

The joint study was used to select the connection architecture for the final boom design. The desired joint was not simply the one with the highest peak force, but the one that most closely preserved homogeneous-beam-like stiffness, strength, and failure behavior.

2.4 Boom Fabrication and Validation Testing

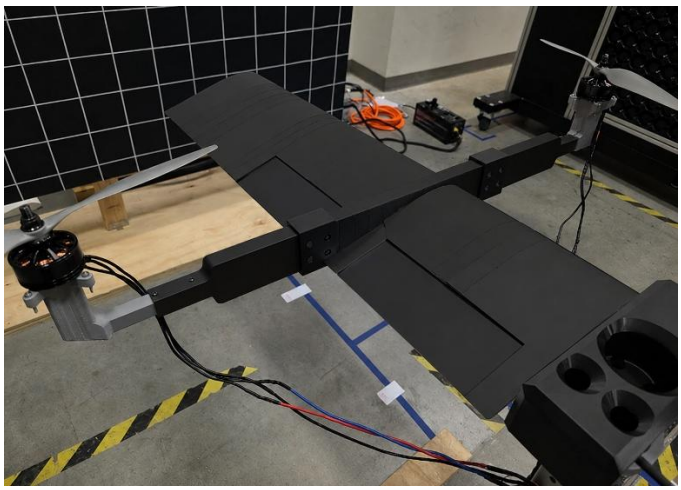


Figure 2.6 – Assembled modular boom installed on the X200 wing structure (VTL boom Design 6 shown on the powered validation setup).

The boom designs were fabricated in PLA using a Bambu H2C printer and sliced in Bambu Studio. Because the topology-optimized and variable-thickness lattice geometries defined the intended internal load path, boom parts were printed at 100% infill rather than using a slicer-generated sparse infill pattern. The printed modules were assembled according to the joint architecture specified for each design iteration and then installed into the X200 wing structure for validation. There were distinct boom design envelopes for designs 1-3 and 4-6 ($l \; x \; w \; x \; h$). For Designs 1-3, the envelope was 31.5 in x 0.91 in x 0.91 in. For Designs 4-6, the envelope was 31.5 in x 0.91 in x 2.25 in.

Boom validation was conducted in two stages. Designs 1–5 were topology-optimized PLA boom concepts evaluated using static loading. For these tests, the X200 wing assembly was inverted and weights were applied at the boom/motor location to represent VTOL thrust loading. The 57.8 N load condition was used as an initial feasibility screen, while the 115.7 N load condition represented the higher-margin validation case. Design 6, the final variable-thickness lattice boom, was evaluated using powered thrust testing on the X200 test fixture.

The boom design iterations 1–5 used topology optimization but varied in joint concept, mass allowance, resulting cross-sectional geometry, and post-processing strategy. Design 6 used the final variable-thickness Kelvin lattice architecture [26] with the pinned sleeve joint selected from the joint test matrix. For powered validation, Design 6 was installed on the X200 test fixture and subjected to motor-driven thrust loading. The boom was tested at 5400 RPM, corresponding to the thrust condition required for X200 VTOL takeoff, and then at 6000 RPM, the maximum motor speed evaluated during the test. This powered validation provided a more realistic propulsion-driven loading condition than static weights alone, although full qualification would require additional static, fatigue, vibration, environmental, and multi-load-case testing.

3. Results

3.1 Joint Screening and Final Joint Selection

The joint screening study showed that modular connection architecture strongly influenced the feasibility of segmented FFF boom structures. In the initial 8 mm joint-length screening tests, several designs provided useful load transfer, but performance was orientation-dependent. In the X orientation,

the strongest modular candidates were the X joint, rotated double lap with two tabs, and pinned sleeve, with structural efficiency index (SEI) values ($\frac{kN^2}{mm}$) of 1.20 × 10⁻⁴, 1.16 × 10⁻⁴, and 1.14 × 10⁻⁴, respectively. In the Y orientation, the rotated double lap with two tabs produced the highest modular-joint SEI, approximately 4.02 × 10⁻⁴, followed by the X joint at approximately 3.15 × 10⁻⁴. The pinned sleeve was lower in the initial 8 mm Y-orientation screening, with an SEI of approximately 1.82 × 10⁻⁴.

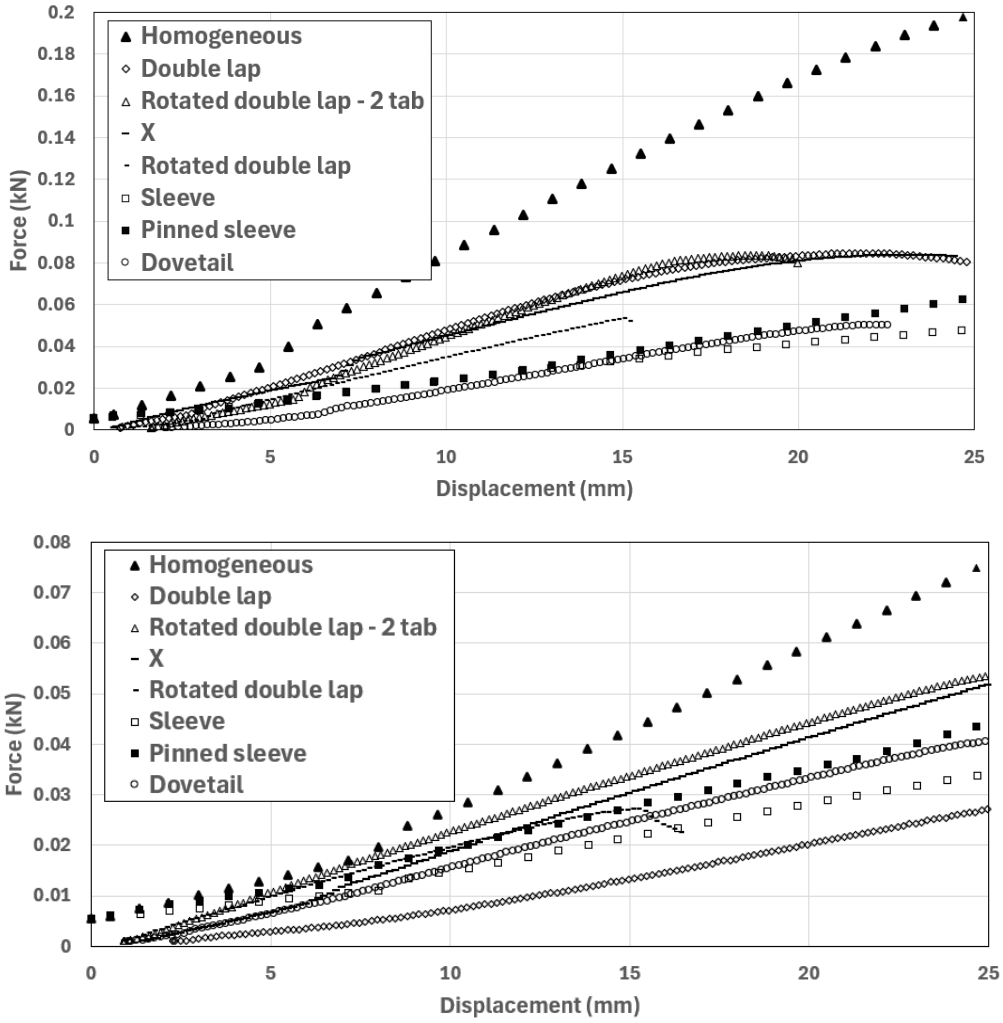


Figure 3.1 – Joint test specimens and representative force-displacement curves for the 8 mm screening study (Top: y-orientation, Bottom: x-orientation).

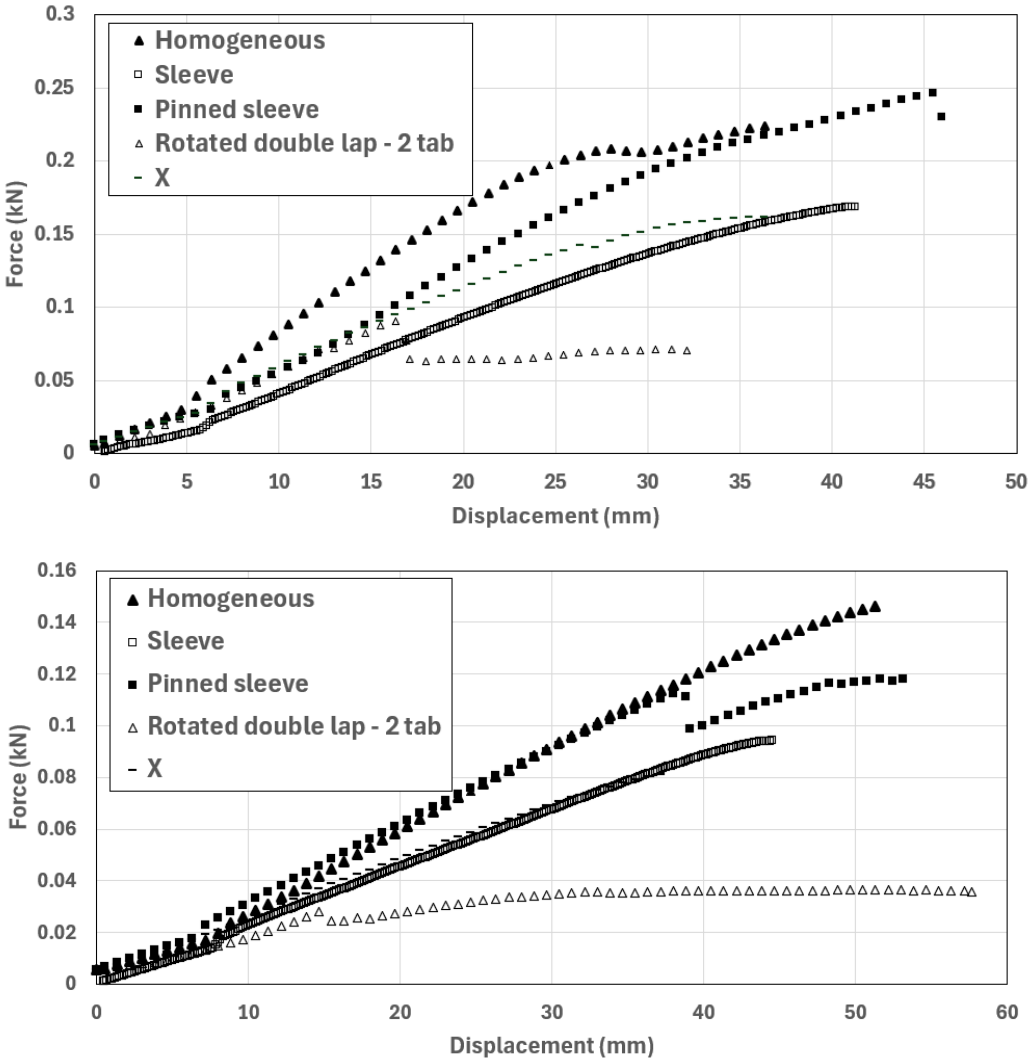


Figure 3.2 – Joint test specimens and representative force-displacement curves for the 18.55 mm screening study (Top: y-orientation, Bottom: x-orientation).

The larger 18.55 mm joint-length retest changed the joint ranking substantially. The pinned sleeve became the strongest overall modular joint candidate, demonstrating that sleeve-supported load transfer benefited from increased engagement length. In the Y-orientation test, the pinned sleeve produced an SEI of approximately 13.0 × 10^{-4}, closely approaching the homogeneous beam value of approximately 13.5 × 10^{-4}. The force-displacement response of the pinned sleeve was nearly coincident with the homogeneous beam curve, indicating that the joint preserved much of the continuous-member stiffness and strength response.

In the X-orientation 18.55 mm test, the homogeneous beam again provided the highest reference value, with an SEI of approximately 4.0 × 10^{-4}. The pinned sleeve was the best modular joint, with an SEI of approximately 2.5 × 10^{-4}, followed by the sleeve at 1.99 × 10^{-4}, the X joint at 1.65 × 10^{-4}, and the rotated double lap with two tabs at 0.23 × 10^{-4}. These results showed that the pinned sleeve was the most balanced joint across both orientations and the only modular design that approached homogeneous-beam behavior in the larger-scale test.

Table 3.1 – Joint SEI summary in the x-orientation.

Joint Design	Joint Length [mm]	Max. Force [kN]	Displacement at Max. Force [mm]	Stiffness [kN/mm]	SEI [kN^2/mm]
Homogeneous	n/a	0.1463	51.3	2.74E-03	4.01E-04
Double lap	8	0.048	56.6	8.65E-04	4.15E-05
Rotated double lap - 2 tab	8	0.0534	24.9	2.18E-03	1.16E-04
X	8	0.0568	27.8	2.12E-03	1.20E-04
Rotated double lap	8	0.0271	15.1	1.84E-03	4.98E-05
Sleeve	8	0.0372	28.8	1.10E-03	4.09E-05
Pinned sleeve	8	0.0702	39.7	1.63E-03	1.14E-04
Dovetail	8	0.0407	25.1	1.65E-03	6.73E-05
Rotated double lap - 2 tab	18.55	0.0365	49.7	6.24E-04	2.28E-05
X	18.55	0.0811	37.2	2.03E-03	1.65E-04
Sleeve	18.55	0.0942	44.5	2.12E-03	1.99E-04
Pinned sleeve	18.55	0.1181	53.1	2.12E-03	2.50E-04

Table 3.2 – Joint SEI summary in the y-orientation.

Joint Design	Joint Length [mm]	Max. Force [kN]	Displacement at Max. Force [mm]	Stiffness [kN/mm]	SEI [kN^2/mm]
Homogeneous	n/a	0.224	36.3	6.01E-03	1.35E-03
Double lap	8	0.0846	22.1	3.91E-03	3.31E-04
Rotated double lap - 2	8	0.0836	18.8	4.80E-03	4.02E-04
X	8	0.0838	22.6	3.76E-03	3.15E-04
Rotated double lap	8	0.0534	15.0	3.74E-03	2.00E-04
Sleeve	8	0.0564	41.3	1.23E-03	6.95E-05
Pinned sleeve	8	0.1091	62.2	1.67E-03	1.82E-04
Dovetail	8	0.0502	22.0	2.46E-03	1.23E-04
Rotated double lap - 2	18.55	0.0713	31.3	2.07E-03	1.48E-04
X	18.55	0.1617	35.5	4.39E-03	7.10E-04
Sleeve	18.55	0.1684	41.1	4.13E-03	6.96E-04
Pinned sleeve	18.55	0.2464	45.5	5.28E-03	1.30E-03

Based on combined stiffness, maximum force, SEI, and failure behavior, the pinned sleeve was selected for the final boom design. The result shows that modular FFF joints require sufficient engagement length and distributed bearing area to avoid becoming the dominant structural weakness.

3.2 Topology-Optimized Boom Iterations

The first five boom designs used the topology optimization workflow to evaluate whether printed PLA could replace the X200 carbon fiber VTOL boom under representative thrust-derived loading. The baseline carbon fiber boom mass was 166 g, including installation bolts. Designs 1–5 progressively varied mass allowance, joint concept, and cross-sectional geometry to identify the features controlling structural performance.

Design 1 was a conservative dovetail-based feasibility concept with a mass of 515 g and was used primarily to evaluate assembly and fit. Design 2 reduced mass to 327 g but failed under the 57.8 N static load condition due to excessive bending and failure at the dovetail joint. Design 3 replaced the

dovetail with a pinned double-lap joint and weighed 358 g. It passed the 57.8 N static load, corresponding to FoS = 2.31, but failed at approximately 89.0 N through pin shear.

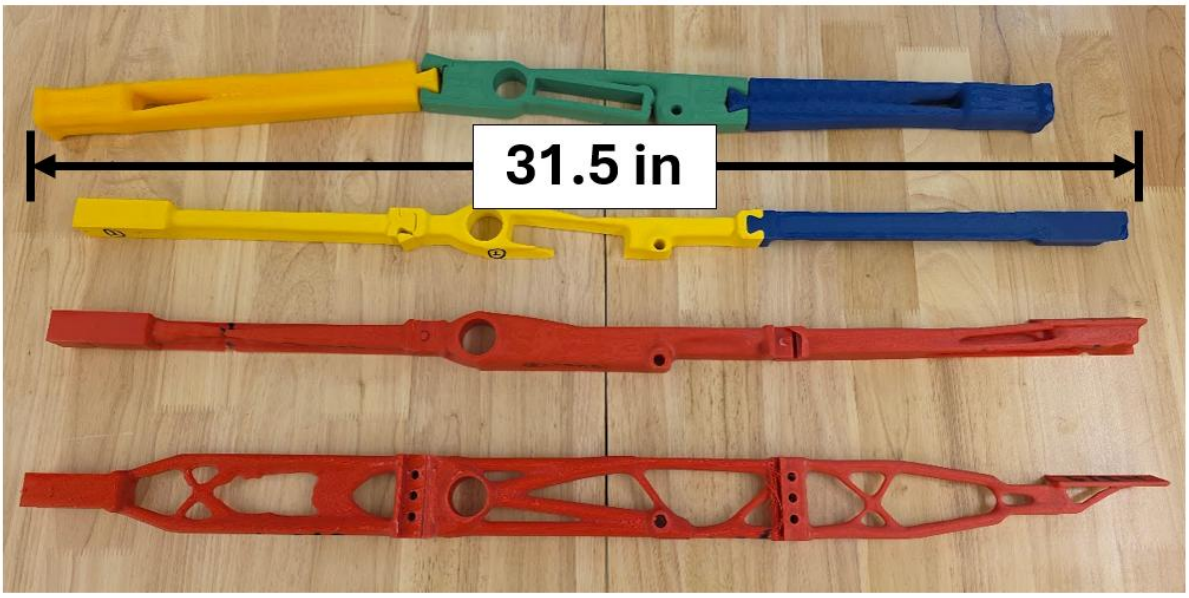


Figure 3.3: Topology-optimized boom design progression for Designs 1–4 (top to bottom).

Design 4 increased the boom cross-sectional height to improve bending resistance through a higher second moment of area (see Fig. 4.2). This design weighed 281 g and successfully supported the 115.7 N static load condition, corresponding to approximately FoS = 4.62. This was the strongest topology-optimized static validation result and demonstrated that a printed PLA boom could achieve a practical structural margin when topology optimization was combined with adequate cross-sectional bending efficiency.

Design 5 retained the increased-height strategy but aggressively reduced mass to 193 g, substantially closer to the 166 g carbon fiber baseline. However, Design 5 failed through lateral rolling during validation. This failure mode was not captured by the initial FEA model, which focused primarily on the maximum-thrust bending case. The result showed that aggressively mass-reduced topology-optimized structures can become sensitive to boundary-condition mismatch and unmodeled off-axis loading [26].

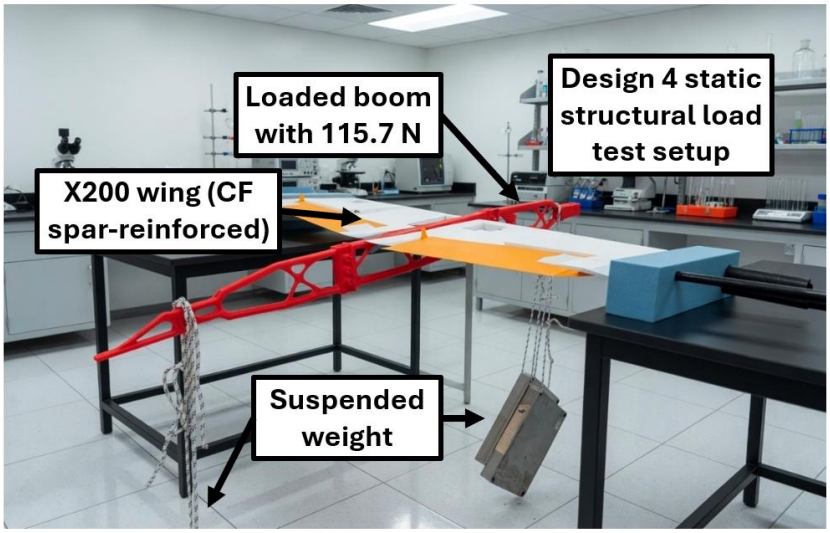


Figure 3.4 – Static structural evaluation with Design 4 passing 115.7 N loading (FoS = 4.62).

Table 3.3 – Optimized boom iteration results.

Boom Design	Optimization Method	Joint Design	Weight [g]*	Pass/Fail	FoS
1	Topology Optimization	Dovetail	515	Fail	n/a
2	Topology Optimization	Dovetail	327	Fail	n/a
3	Topology Optimization	Pinned double lap	358	Pass	2.31
4	Topology Optimization	Pinned double lap	281	Pass	4.62
5	Topology Optimization	Pinned double lap	193	Fail	n/a
6	Variable-Thickness Lattice	Pinned sleeve	218	Pass	n/a**

* Weight of the carbon fiber boom was 166g.

** Different test for design 6 did not allow for comparable FoS evaluation.

Overall, the topology-optimized boom sequence demonstrated that TO can produce a structurally viable printed boom, but only when joint architecture and cross-sectional bending efficiency are sufficient. The failure of Design 5 motivated the transition to a variable-thickness lattice architecture for the final design.

3.3 Final VTL Boom Validation

The final boom design, Design 6, used a variable-thickness Kelvin lattice rather than a sparse topology-optimized internal structure. This design retained the elevated cross-sectional strategy that improved Design 4, incorporated the pinned sleeve joint selected from the larger-scale joint study, and used a stress-field-driven lattice thickness distribution to improve load-path redundancy. The lattice had a 30 mm × 30 mm × 30 mm unit cell, 0.8 mm minimum member thickness, 5 mm maximum member thickness, and a 1 mm exterior shell.

Design 6 had a final mass of 217 g. This was lighter than the successful static TO Design 4 but heavier than the aggressively reduced TO Design 5 and the 166 g carbon fiber baseline. Relative to the carbon fiber boom, Design 6 had a mass increase of 51.6 g, or approximately 31%. Therefore, the final design was not mass-equivalent to carbon fiber, but it represented the most robust printed boom architecture evaluated in this study.

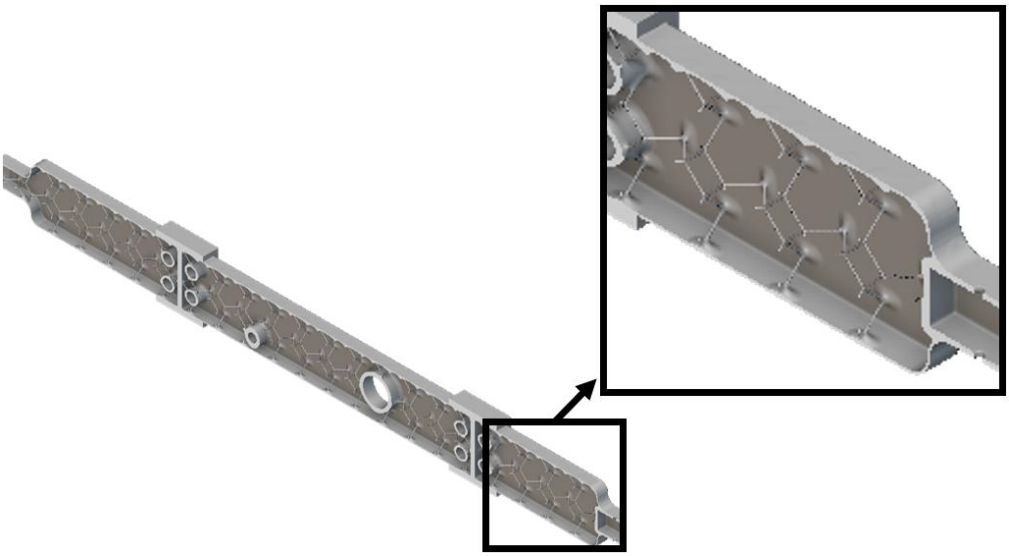


Figure 3.5 – Cross section of the final Design 6 variable-thickness lattice boom with the pinned sleeve joint and Kelvin lattice structure.

Design 6 was validated using powered thrust testing rather than dead-weight static loading. The boom was installed on the X200 test fixture and tested at 5400 RPM, corresponding to the thrust condition required for X200 VTOL takeoff. The test was then increased to 6000 RPM, the maximum motor speed evaluated during validation. The VTL boom successfully passed both powered thrust conditions without observed structural failure.

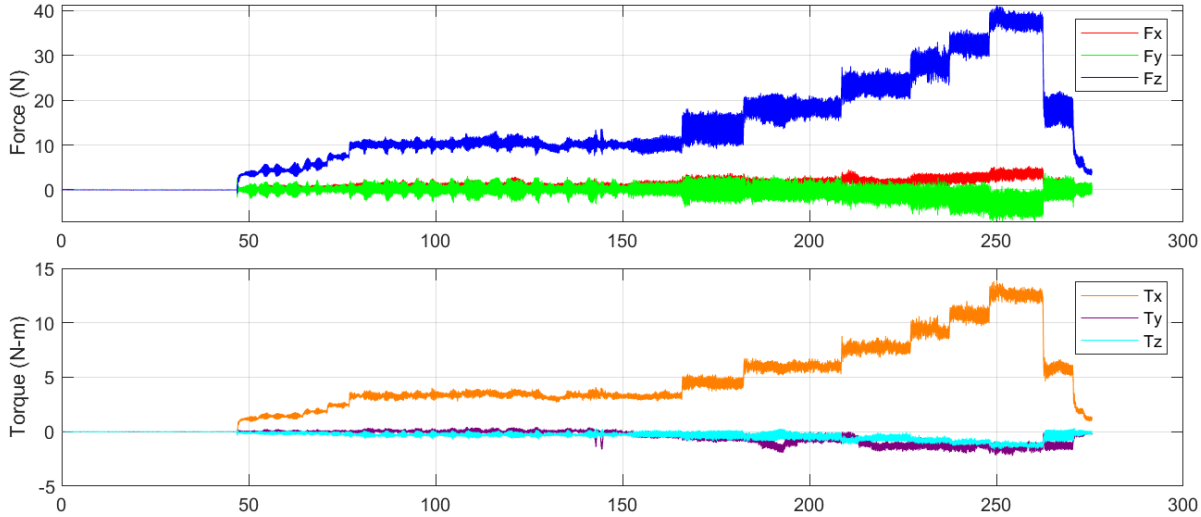


Figure 3.6 – Thrust and torque data for ramped RPM for the VTL boom Design 6 (as a function of time [s]).

The final VTL result demonstrates that modular FFF boom replacement is feasible for the evaluated X200 powered VTOL condition when the design combines three features: a robust pinned sleeve joint, bending-efficient cross-sectional geometry, and distributed lattice reinforcement. However, the remaining mass gap and the difference between static and powered validation methods indicate that additional optimization and testing are required before the printed boom can be considered a viable carbon fiber replacement.

4. Discussion

4.1 Joint Architecture Enables Modular FFF Structures

The results show that joint architecture is a controlling design variable for modular FFF UAV structures. Because the optimized boom geometries exceeded the available printer build volume, segmentation was necessary. However, segmentation introduces interfaces where local rotation, bearing damage, stress concentration, and slip can dominate the structural response. Therefore, the printed boom cannot be evaluated only as an optimized body; the assembled structure is only viable if the joints preserve load transfer across the segmented member.

The joint screening study demonstrated this clearly. Several compact 8 mm joints performed well in selected orientations, but the larger 18.55 mm tests showed that engagement length strongly affected joint behavior. The pinned sleeve became the best overall modular joint because it combined distributed sleeve contact with positive mechanical locking. In the Y-orientation larger-scale test, its force-displacement response was nearly coincident with the homogeneous beam, and its SEI approached the homogeneous reference value. This suggests that the pinned sleeve distributed load sufficiently well that the specimen behaved more like a continuous member than a segmented assembly.



Figure 4.1 – Pinned sleeve failure mode relative to the homogeneous beam in X and Y orientations.

The boom-level results support this interpretation. The dovetail joint was useful for alignment and assembly, but it failed under boom-level bending in Design 2. The pinned double-lap joint improved performance in Designs 3 and 4, but pin shear and off-axis sensitivity remained concerns. The pinned sleeve was therefore selected for the final VTL boom because it provided the best balance of stiffness, strength, manufacturability, and homogeneous-beam-like response. These results indicate that modular FFF structures require joints to be designed as structural load-transfer features.

4.2 Geometry and Load-Case Sensitivity Govern Printed Boom Performance

The topology-optimized boom iterations demonstrated that printed PLA can provide a practical structural margin when the geometry is designed around the governing mechanics. Design 4 passed the 115.7 N static load condition, corresponding to approximately FoS = 4.62, despite the lower stiffness and strength of PLA relative to carbon fiber. This result is significant because the goal was not to match the excessive reserve capacity of the carbon fiber baseline, but to determine whether a printed boom could provide a mission-sufficient structural margin.

The success of Design 4 was strongly related to the cross-sectional bending efficiency. The X200 boom is primarily bending loaded under VTOL thrust, so increasing the second moment of area was critical. This behavior is consistent with the bending stress relationship,

$$\sigma = \frac{Mc}{I} \tag{5}$$

where increasing I reduces bending stress for a given moment. Since PLA cannot match carbon fiber by material properties alone, the printed design must use geometry to recover performance. Design 4 showed that a higher section geometry provides practical strength to aid in the mechanical property difference.

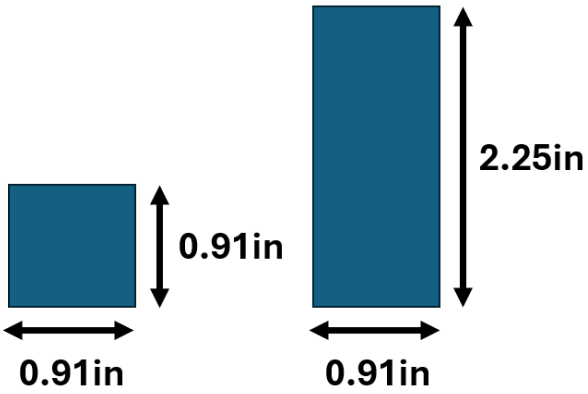


Figure 4.2 – Cross-sectional comparison quantifying the increased height and the improved flexural rigidity from Design 1-3 to Designs 4-6.

However, Design 5 showed the limit of aggressive single-load-case topology optimization. Although its mass was reduced to 193 g, much closer to the 166 g carbon fiber baseline, it failed by lateral rolling. This failure mode was not predicted by the initial FEA model, which focused primarily on maximum vertical thrust bending. The result indicates that sparse topology-optimized structures can become overly tuned to the prescribed boundary conditions and may lose robustness to secondary modes such as torsion, lateral bending, asymmetric thrust, joint rotation, and fixture-induced loads.

Thus, topology optimization is feasible for printed UAV boom design, but only when the load envelope is complete enough for the desired mass target. At moderate mass reduction, the method identified useful load paths and produced a boom that passed the target static load. At more aggressive mass reduction similar to that of the carbon fiber boom, the omitted off-axis load modes became structurally critical. Future TO-based designs should therefore use multi-load-case optimization rather than a single maximum-thrust bending case.

4.3 VTL Robustness and Carbon Fiber Mass Gap

The final VTL boom addressed the main limitation observed in the topology-optimized design: insufficient load-path redundancy. Instead of reducing the boom to a sparse set of optimized members, the variable-thickness Kelvin lattice preserved repeated internal load paths while still using the FEA-derived stress field to vary material placement. Higher-stress regions received thicker members, while lower-stress regions retained thinner members. This strategy allowed the design to combine bending-efficient external geometry with distributed internal reinforcement. The bending advantage is supported by the parallel axis theorem, $I = I_c + Ad^2$, which shows that a material area A contributes to the second moment of area in proportion to the square of its distance $d$from the neutral axis. Thus, material placed near the outer envelope is far more effective in increasing flexural rigidity (*EI*) than material located near the neutral axis.

This architecture is also consistent with lightweight structural strategies observed in avian morphology. Bird bones do not generally achieve low mass by reducing structure to a few isolated members; rather, they place much of the load-bearing material near the outer wall while using internal randomized lattice reinforcement to stabilize the section and redistribute load. The VTL boom follows a similar mechanical principle by using an efficient outer section for bending stiffness and an internal lattice for load redistribution and buckling resistance. This differs from sparse topology optimization, which can remove stabilizing material that is not highly stressed in the prescribed load case but may still be important for off-axis stiffness, local stability, and damage tolerance. This redundancy is particularly useful for FFF structures, where local print defects, layer bonding variability, and anisotropic properties can make any single printed load path even less reliable.

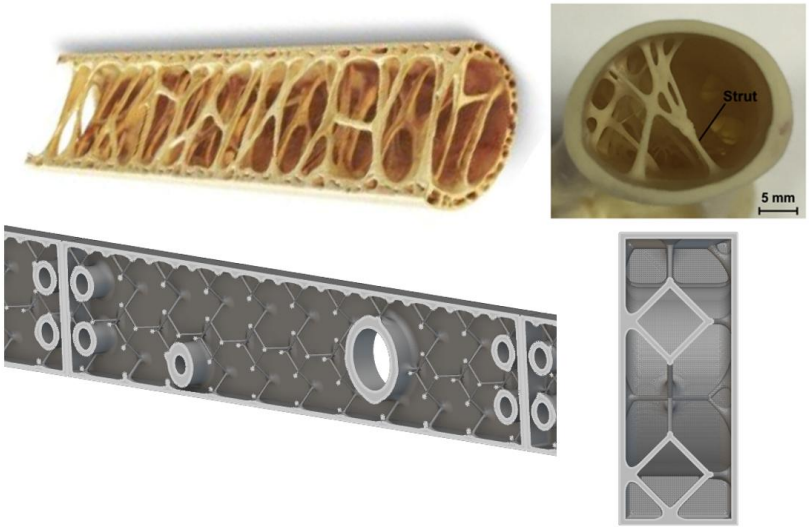


Figure 4.3 – Comparison of VTL boom architecture and avian bone morphology [25,26].

Design 6 validated this approach under powered thrust testing. The final VTL boom weighed 218 g and passed both 5400 RPM, corresponding to the X200 VTOL takeoff condition, and 6000 RPM, the maximum tested motor speed. This result suggests that a modular FFF boom can function under representative powered loading when joint architecture, cross-sectional geometry, and internal lattice redundancy are treated as coupled design variables.

However, the final VTL boom remained heavier than the 166 g carbon fiber baseline by 51.6 g, or approximately 31%. Therefore, the current design should be interpreted as a feasibility demonstration rather than a mass-equivalent carbon fiber replacement. This mass gap is expected because PLA has lower stiffness and strength than carbon fiber, requiring additional geometric efficiency, local reinforcement, or internal structure to reach the required load margin.

The implication is that carbon fiber replacement should be framed as mission-sufficient structural replacement rather than direct material substitution. If the original carbon fiber member is substantially overdesigned for the evaluated operating condition, then a printed polymer replacement may be acceptable without matching carbon fiber's full reserve capacity. For research, prototyping, and field-repair applications, the value of modular FFF also includes rapid fabrication, reduced tooling, simplified replacement, and design iteration speed in addition to structural performance.

4.4 Limitations

This study has several limitations. First, the finite element model focused primarily on the maximum VTOL thrust bending case and did not fully include torsion, asymmetric thrust, lateral acceleration, vibration, landing, recovery, or handling loads. The Design 5 lateral rolling failure shows that these secondary load modes can become important as mass is reduced. Second, the PLA material model was homogenized and orthotropic, but it did not explicitly capture bead-scale defects, interlayer weld quality, voids, residual stress, or progressive damage. Third, only PLA was evaluated, so the results should not be interpreted as final flight-ready material selection.

PLA was selected as the baseline material because it prints reliably, provides good dimensional consistency, and allowed the study to isolate the effects of geometry, joint architecture, and lattice redundancy without introducing additional material-processing variables. The results should therefore be interpreted as a conservative feasibility demonstration rather than a final material selection. Higher-performance materials such as PETG, ASA, nylon-based polymers, or CF-reinforced PLA may reduce the remaining 31% mass gap by improving stiffness, toughness, thermal resistance, or specific strength. However, each material also introduces new tradeoffs in printability, anisotropy, interlayer bonding, support removal, environmental durability, and cost. Future work will evaluate these material upgrades after joint robustness, section efficiency, and lattice redundancy are fully established.

A further limitation is that Design 6 was validated using powered thrust testing rather than the same static dead-weight protocol used for Designs 1–5. The powered test was more representative of propulsion-driven loading, but it limits direct load-to-load comparison with the earlier static tests. Future work should apply both static and powered validation to the same final geometry. In addition, fatigue, vibration, environmental exposure, repeated assembly/disassembly, joint wear, and post-test microscopy or microCT were outside the scope of the current work.

These limitations do not negate the feasibility demonstrated by Design 6, but they define the next steps required to mature the method. The present work shows that modular FFF boom replacement can carry representative X200 VTOL loading when designed around joint robustness, bending efficiency, and lattice redundancy. Full qualification will require expanded loading, improved materials, mass optimization, and durability testing.

5. Conclusions and Future Work

This study evaluated a modular fused filament fabrication workflow for replacing the carbon fiber VTOL boom structure of an X200 Group 2 eVTOL hybrid UAV. The work was motivated by a preliminary structural case study showing that the existing carbon fiber boom had an excessive factor of safety.

Therefore, the printed boom was not intended to reproduce the full reserve capacity of the carbon fiber member, but to determine whether a mission-sufficient printed polymer structure could achieve a more practical design margin while improving manufacturability, modularity, and repairability.

The following conclusions were drawn from this study:

1. **The X200 carbon fiber boom was a strong candidate for mission-sufficient replacement.**
The estimated carbon fiber boom factor of safety indicated substantial overdesign for the evaluated VTOL loading condition. This created an opportunity to investigate printed polymer replacement at a more practical target margin of approximately FoS = 3–7.

2. **Joint architecture controlled the feasibility of modular FFF boom structures.**
The joint study showed that segmentation cannot be treated as only a manufacturing constraint. The pinned sleeve joint provided the best large-scale modular response and approached homogeneous-beam behavior in the 18.55 mm Y-orientation test, making it the most suitable joint for the final boom design.

3. **Topology optimization produced a viable printed boom, but only when paired with sufficient bending efficiency.**
Design 4, a topology-optimized PLA boom with increased section height, successfully supported the 115.7 N static load condition, corresponding to approximately FoS = 4.62. This demonstrated that printed PLA can meet a practical structural margin when geometry is used to compensate for lower material stiffness and strength.

4. **Aggressive topology optimization introduced boundary-condition sensitivity.**
Design 5 reduced the boom mass to 193 g, closer to the 166 g carbon fiber baseline, but failed through lateral rolling. This failure mode was not captured by the initial maximum-thrust bending model, showing that mass-reduced TO designs require expanded multi-load-case analysis prior to optimization and subsequent manufacturing.

5. **Variable-thickness lattice design improved robustness through load-path redundancy.**
The final Design 6 boom used a Kelvin variable-thickness lattice, elevated cross-sectional geometry, and a pinned sleeve joint. It successfully passed powered thrust testing at both 5400 RPM, corresponding to the X200 VTOL takeoff condition, and 6000 RPM, the maximum tested motor speed.

6. **The final printed boom was feasible but not yet mass-equivalent to carbon fiber.**
Design 6 weighed 218 g, approximately 31% heavier than the 166 g carbon fiber baseline. The result should therefore be interpreted as a feasibility demonstration rather than a fully optimized carbon fiber-equivalent replacement.

Future work will focus on closing the carbon fiber mass gap while expanding the validation envelope. The next boom iterations should reduce mass through cross-sectional geometry optimization, lattice-parameter refinement, and minimum-mass pinned sleeve design. Candidate boom sections should include filleted rectangular, elliptical, and airfoil-like geometries that preserve second moment of area while reducing unnecessary volume. The variable-thickness lattice should also be optimized for unit cell size, shell thickness, minimum member thickness, maximum member thickness, and local reinforcement near joints and mounting regions.

Future finite element work should expand beyond the single maximum-thrust bending case. The Design 5 lateral rolling failure showed that secondary load modes become important as mass is reduced. Future models should include torsion from motor torque, lateral bending, asymmetric thrust, vibration, handling loads, recovery loads, and combined load cases. These load cases should be incorporated directly into multi-load-case optimization so that material is not removed from regions needed for off-axis stability.

Future experimental work should apply both static and powered validation to the same final geometry. Design 6 passed powered thrust testing, while Designs 1–5 were evaluated primarily by static

loading. Testing both methods on the same design would allow direct comparison between dead-weight structural capacity and propulsion-driven load transfer. Additional validation should include fatigue testing, vibration/modal testing, environmental exposure, repeated assembly/disassembly, joint durability, and post-test microscopy or microCT to identify failure initiation mechanisms.

Spar redesign will be addressed as a separate future study. The spar replacement problem will require a dedicated cross-sectional flexural rigidity study to evaluate FFF-compatible spar geometries. Candidate spar sections should be assessed using EI, where E is the effective orthotropic modulus of the printed material and I is the second moment of area. Because printed polymers have lower modulus than carbon fiber composites, geometry must be used to recover bending stiffness. However, thin-wall high-I sections may become susceptible to local buckling before reaching global yielding or bending failure. Future spar work must therefore balance flexural rigidity, local buckling resistance, torsional stiffness, printability, mass efficiency, and modular joint integration.

Overall, this work demonstrates that modular FFF structures can serve as mission-sufficient replacements for selected overdesigned carbon fiber UAV components. The final VTL boom did not yet match the carbon fiber mass, but it successfully carried the representative X200 powered VTOL thrust condition. With further mass optimization, expanded load-case modeling, improved material selection, and durability validation, modular printed structures may provide a practical pathway for rapid Group 1–2 UAV structural development.

Acknowledgments

This work was supported by the Oklahoma State University Engineering Research and Seed Funding Program performed at the Helmerich Research Center. The authors also want to acknowledge the contributions of students involved in part testing and additive manufacturing process development, including Pratibha Bhandari and Daniela Durango-Cueva.

Contact Author Email Address

chrsc@okstate.edu

Copyright Statement

The authors confirm that they, and/or their company or organization, hold copyright on all of the original material included in this paper. The authors also confirm that they have obtained permission, from the copyright holder of any third party material included in this paper, to publish it as part of their paper. The authors confirm that they give permission, or have obtained permission from the copyright holder of this paper, for the publication and distribution of this paper as part of the ICAS proceedings or as individual off-prints from the proceedings.

References

[1] Yap Y L, Toh W, Giam A, Yong F R, Chan K I, Tay J W S, Teong S S, Lin R and Ng T Y. Topology optimization and 3D printing of micro-drone: numerical design with experimental testing. *International Journal of Mechanical Sciences*, Vol. 237, 107771, 2023.

[2] Bronz M, Tal E, Favalli F and Karaman S. Mission-oriented additive manufacturing of modular mini UAVs. Proc AIAA Scitech 2020 Forum, Orlando, FL, USA, paper no. AIAA 2020-0064, 2020.

[3] Banfield C P, Kidd J and Jacob J D. Design and development of a 3D printed unmanned aerial vehicle. Proc AIAA Aviation 2016 Forum, paper no. AIAA 2016-2029, 2016.

[4] Chung S-H, Ma D-M and Shiau J-K. Design, manufacturing, and flight testing of an experimental flying wing UAV. *Applied Sciences*, Vol. 9, No. 15, 3043, 2019.

[5] MohamedZain A O, Chua H, Yap K, Uthayasurian P and Jiehan T. Novel drone design using an optimization software with 3D model, simulation, and fabrication in drone systems research. *Drones*, Vol. 6, No. 4, 97, 2022.

[6] Šostakaitė L, Šapranauskas E, Rudinskas D, Rimkus A and Gribniak V. Investigating additive manufacturing possibilities for an unmanned aerial vehicle with polymeric materials. *Polymers*, Vol. 16, No. 18, 2600, 2024.

[7] Chatzopoulos A, Kantaros A, Zacharia P, Ganetsos T and Papoutsidakis M. A 3D-printed, open source, low-cost drone platform for mechatronics and STEM education in an academic context. *Drones*, Vol. 9, No. 11, 797, 2025.

[8] Al-Hadithi B M and Alcón Flores S. Design and validation of a 3D-printed drone chassis model through static and transient nonlinear FEM analyses and experimental testing. *Drones*, Vol. 9, No. 11, 789, 2025.

[9] Balayan A, Mallick R, Dwivedi S, Saxena S, Haorongbam B and Sharma A. Optimal design of quadcopter chassis using generative design and lightweight materials to advance precision agriculture. *Machines*, Vol. 12, No. 3, 187, 2024.

[10] Muralidharan N, Pratheep V G, Shanmugam A, Hariram A, Dinesh P and Visnu B. Structural analysis of mini drone developed using 3D printing technique. *Materials Today: Proceedings*, Vol. 46, pp 8748-8752, 2021.

[11] Shelare S D, Aglawe K R and Khope P B. Computer aided modeling and finite element analysis of 3-D printed drone. *Materials Today: Proceedings*, Vol. 47, pp 3375-3379, 2021.

[12] Pecho P, Bugaj M, Kulíšková M, Sooš L, Varga J and Novák M. Experimental analysis of 3D-printed wing's deformation under various load distribution. *Transportation Research Procedia*, Vol. 40, pp 861-868, 2019.

[13] Huang Y, Tian X, Li W, He S, Zhao P, Hu H, Jia Q and Luo M. 3D printing of topologically optimized wing spar with continuous carbon fiber reinforced composites. *Composites Part B: Engineering*, Vol. 272, 111166, 2024.

[14] Goh G D, Agarwala S, Goh G L, Dikshit V, Sing S L and Yeong W Y. Additive manufacturing in unmanned aerial vehicles (UAVs): challenges and potential. *Aerospace Science and Technology*, Vol. 63, pp 140-151, 2017.

[15] Comer A, Bhandari R, Putra S H and Chakraborty I. Design, control law development, and flight testing of a subscale lift-plus-cruise aircraft. Proc AIAA SCITECH 2024 Forum, Orlando, FL, paper no. AIAA 2024-2644, 2024.

[16] Comer A, Atkinson Z, Bhandari P, Miller Z and Harp E. Development of a simulation to flight workflow for subscale flight testing of experimental control laws. Proc AIAA SCITECH 2026 Forum, Orlando, FL, paper no. AIAA 2026-2063, 2026.

[17] Comer A, Chakraborty I, Putra S, Bhandari R and Kunwar B. Flight testing a trajectory control system on a subscale transitioning VTOL aircraft. *Journal of Guidance, Control, and Dynamics*, 2025.

[18] Müller T and Gollnick V. Building methods for a composite constructed VTOL using 3D printing techniques. Proc 34th Congress of the International Council of the Aeronautical Sciences, Florence, Italy, paper no. ICAS2024_0313, 2024.

[19] Baltić M Z, Vasić M R, Vorkapić M D, Bajić D M, Piteľ J, Svoboda P and Vencl A. PETG as an alternative material for the production of drone spare parts. *Polymers*, Vol. 16, No. 21, 2976, 2024.

[20] García-Tíscar J, Quintero P, Ramírez F N and Cremades A. Effect of popular additive manufacturing techniques on performance and acoustics of UAV propellers. Proc 34th Congress of the International Council of the Aeronautical Sciences, Florence, Italy, paper no. ICAS2024_0896, 2024.

[21] Gonzalo J, López D, Domínguez D, García A and Escapa A. On the capabilities and limitations of high altitude pseudo-satellites. *Progress in Aerospace Sciences*, Vol. 98, pp 37-56, 2018.

[22] Vanwagenen R. *A guide to structural factors for advanced composites used on spacecraft*. NASA Technical Memorandum 102209, National Aeronautics and Space Administration, 1989.

[23] Andries V and Zaharia S-M. Generative design, simulation, and 3D printing of the quadcopter drone frame. *Applied Sciences*, Vol. 15, No. 17, 9647, 2025.

[24] Guessasma S, Belhabib S and Nouri H. Printability and tensile performance of 3D printed PETG using fused deposition modelling. *Polymers*, Vol. 11, No. 7, 1220, 2019.

[25] Sullivan T N et al. Extreme lightweight structures: avian feathers and bones. *Materials Today*, 2017.

[26] Scott, C., Comer, A., and Hanan, J. Comparative Evaluation of Finite Element-Driven Optimization Methods for Additively Manufactured UAV Primary Structures. Proceedings of the Vertical Flight Society 82nd Annual Forum & Technology Display, West Palm Beach, FL, May 2026.